nature physics

LETTERS

https://doi.org/10.1038/s41567-018-0150-8

Topological kinematics of origami metamaterials

Bin Liu[1,2,8*], Jesse L. Silverberg[1,3,4,8], Arthur A. Evans[5], Christian D. Santangelo[5], Robert J. Lang[6], Thomas C. Hull[7] and Itai Cohen[1]

A variety of electronic phases in solid-state systems can be understood by abstracting away microscopic details and refocusing on how Fermi surface topology interacts with band structure to define available electron states[1]. In fact, topological concepts are broadly applicable to non-electronic materials and can be used to understand a variety of seemingly unrelated phenomena[2–6]. Here, we apply topological principles to origami-inspired mechanical metamaterials[7–12], and demonstrate how to guide bulk kinematics by tailoring the crease configuration-space topology. Specifically, we show that by simply changing the crease angles, we modify the configuration-space topology, and drive origami structures to dramatically change their kinematics from being smoothly and continuously deformable to mechanically bistable and rigid. In addition, we examine how a topologically disjointed configuration space can be used to constrain the locally accessible deformations of a single folded sheet. While analyses of origami structures are typically dependent on the energetics of constitutive relations[11–14], the topological abstractions introduced here are a separate and independent consideration that we use to analyse, understand and design these metamaterials.

For our purposes, we define origami-inspired mechanical metamaterials as materials constructed from a series of torsional creases embedded within a thin sheet[15]. Each crease adds a degree of freedom (DOF) and increases the dimensionality of the configuration space. Each crease intersection, or vertex, generates geometric constraints and limits the available portion of configuration space[16,17]. A folded structure then occupies a single point in this configuration space, and in the same way the Fermi surface topology defines nearby accessible electron states, the configuration space's topology defines nearby accessible folding configurations. By introducing constraints on folding angles, the connectivity of the configuration-space topology can be substantially altered. As such, this coupling between folding angles and configuration-space topology allows for unusual kinematic phenomena to emerge.

To understand the significance of this point, we should clearly distinguish the roles played by energetics and configuration-space topology in the context of origami-inspired metamaterials. We examine these differences through the lens of bistability, which is a common phenomenon to many origami structures[16,18–21] (Fig. 1a). On the one hand, a purely energetic bistability appears when the configuration space is simply connected and there are two distinct local energy minima (Fig. 1a, left). Origami-inspired structures assembled from rigid panels and torsional springs can exhibit this type of energetic bistability (Fig. 1b)[19,22]. On the other hand, a purely topological bistability appears when the configuration space is no longer simply connected, and there exist distinct configurations that are inaccessible from one another (Fig. 1a, right). Both energetic and topological bistabilities allow for multiple configurations. However, the origins of these bistabilities are quite

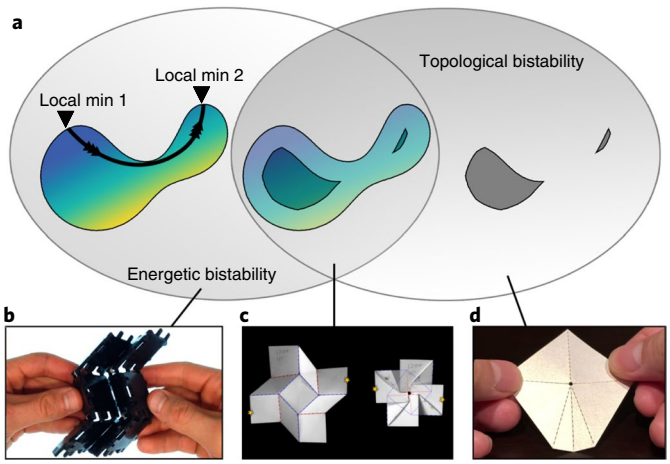

Fig. 1 | Distinguishing the roles of topological and energetic considerations in origami mechanics. a, Venn diagram illustrating the differences and relationship between energetic and topological bistability. An energetic bistability (left) arises when a simply connected configuration space (coloured region; energetic landscape indicated by colouring, with yellow being high-energy and blue being low-energy) contains two energetic minima (blue areas indicated by arrows). A topological bistability (right) arises when the configuration space is disconnected and no path exists that connects these two regions (isolated grey shapes). Many origami structures have their mechanics arising from both topological and energetic considerations (middle). In particular, a topological bistability defined by the crease geometry can be bridged by bending deformations that cost energy (blue-to-yellow coloured region connecting topologically isolated regions). **b**, An example of an origami-inspired pure-energetic bistability with multiple stable states accessible through changes to the folding angles in a simply connected configuration space. **c**, A common example of an origami structure whose unfolded and folded configurations are topologically disconnected when only considering crease DOFs[16]. The introduction of mechanical bending adds additional DOFs at an energetic cost that bridges the two configurations. **d**, An example structure considered here with a tuneable topological bistability. Credit: courtesy of S. Waitukaitis, P. Dieleman and M. van Hecke (**b**).

[1]Department of Physics, Cornell University, Ithaca, NY, USA. [2]School of Natural Sciences, University of California, Merced, Merced, CA, USA. [3]Wyss Institute for Biologically Inspired Engineering, Harvard University, Boston, MA, USA. [4]Department of Systems Biology, Harvard Medical School, Boston, MA, USA. [5]Department of Physics, University of Massachusetts Amherst, Amherst, MA, USA. [6]Lang Origami, Alamo, CA, USA. [7]Department of Mathematics, Western New England University, Springfield, MA, USA. [8]These authors contributed equally: Bin Liu, Jesse L. Silverberg.
*e-mail: bliu27@ucmerced.edu

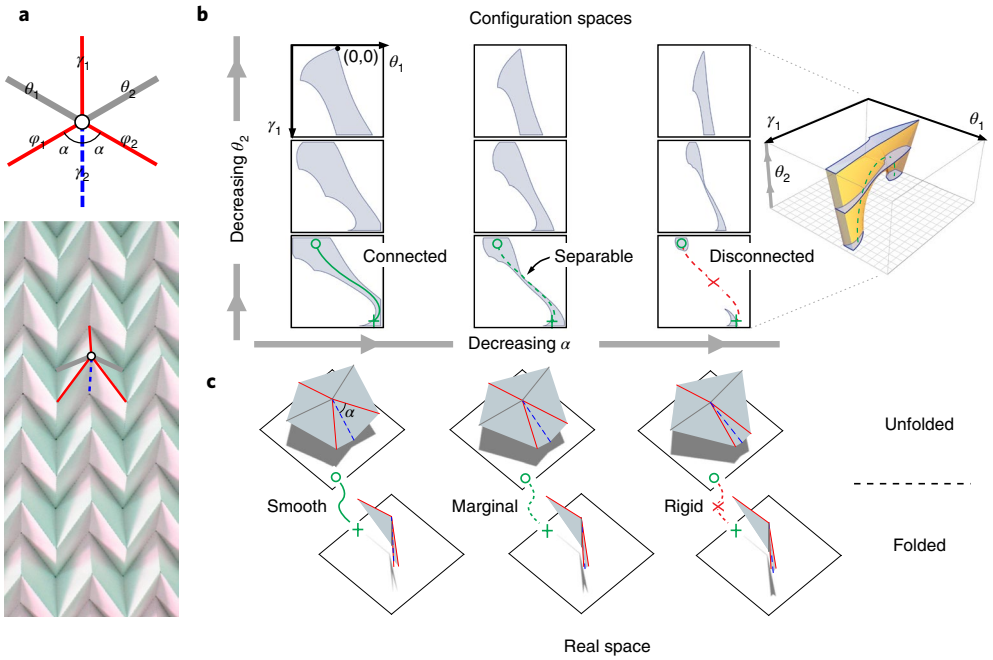

Fig. 2 | Configuration-space topology of origami-inspired mechanical metamaterials is determined by the underlying crease pattern. a, A triangulated Miura-ori vertex has four creases (three mountain folds in solid red and one valley fold in dashed blue) and two additional crease-like hinges that come from the thin sheet's flexibility (grey lines). In this symmetric Miura-ori vertex, the plane angle α parameterizes the folding pattern. The photograph below shows the folded structure colour-coded by the above crease pattern. **b**, Configuration spaces for varying plane angle α and fold angle θ_2. In each $\langle\theta_1, \gamma_1\rangle$ configuration space, the allowed configurations are grey and the forbidden configurations are white, similar to Fig. 1. As α and θ_2 vary, the configuration-space topology can change from one continuously connected region to two disconnected regions. The 3D diagram shows the configuration space of the right-most column and indicates the three cuts with monostable, separable and disconnected domains. **c**, The real-space 3D structures for the bottom row of the configuration spaces in **b**. The folding actuation varies from smooth (monostable) to rigid (bistable) as the configuration space goes from connected to disconnected (Supplementary Movie 1).

different: an energetic bistability is rooted in the material properties that determine the cost of moving through configuration space, while a topological bistability is rooted in the connectivity between available configurations with no regard for material properties. While this theoretical abstraction is quite precise, many experimental origami structures convolve these effects. As a result, we often find topological bistabilities in crease patterns that are connected by hidden DOFs such as facet bending (Fig. 1c). In these cases, energetics bridge a topological bistability through the interplay between crease geometry and the mechanics of bending (Fig. 1a, middle). Here, we broadly disregard energetic considerations relating to hidden DOFs, and instead focus strictly on the phenomena that emerge from the dynamics of configuration space topology. While physical materials will always have some amount of hidden DOFs that play into the bulk mechanical properties, the study of configuration space itself uncovers a variety of new insights regarding vertex–vertex coupling and its ability to mediate non-local influence through dynamic constraints on the global configuration space.

Origami metamaterials are typically designed by tessellating individual units[19,23,24]. Before we address these more complex systems, we first analyse the configuration-space topology of a single vertex (Fig. 1d). For example, we extract a single vertex from a triangulated Miura-ori pattern[25] parametrized by folding angle α and analyse its configuration space. The vertex has four prescribed creases with non-zero preferred rest angles (three mountain folds ϕ_1, ϕ_2, $\gamma_1 < 0$ rad, and one valley fold $\gamma_2 > 0$ rad) and two virtual creases (θ_1, θ_2) with zero preferred rest angle (Fig. 2a). A Miura-ori vertex without virtual creases has only one DOF, which we choose here to be γ_1. Triangulating the folding pattern introduces two extra DOFs to the configuration space. For a range of α, we find the three-dimensional (3D) configuration space of the vertex is simply connected (Fig. 2b, left column), and the resulting kinematics demonstrate smooth actuation (Fig. 2c, left column). As we decrease α, the configuration-space topography narrows, with all pathways between the initial and final configurations passing through a single point in configuration space. This marginal actuation (Fig. 2b, middle column) is smooth but tightly constrained (Fig. 2c, middle column). As we continue to decrease α, the configuration topology becomes disconnected for θ_2 larger than a critical value (Fig. 2b, right column; see Supplementary Information). For fixed θ_2, we find that varying α breaks configuration-space homotopy[26] (Fig. 2b, bottom row), and the disconnection results in bistable systems (Fig. 2c, right). As demonstrated by the isolated vertex, configuration-space topology has both qualitative and quantitative effects for the real-space kinematics (Supplementary Movie 1).

In a multi-vertex folding pattern, the configuration-space dimensionality is larger than the isolated vertex just considered. As a result, the folding of a crease in one region of the structure can change the global configuration-space topology, affecting the folding behaviour in another region of the structure. This interplay allows for the potential to design multiple distinct mechanical functionalities into the global behaviour of a single folding sheet. To illustrate this principle, we connected vertices in a series of concentric Miura-ori-like rings (Fig. 3a), which bears similarities to artistic origami structures[27,28]. Here, we consider only the vertices along the radial direction due to the azimuthal symmetry, and we permit creases to fold only in the prescribed directions. When the structure begins to fold from a flat sheet, each vertex initially has a continuously connected configuration space. As long as the innermost vertex remains unfolded, the entire structure remains only moderately constrained and flexible. However, as the innermost ring folds, it constrains the neighboring ring to a configuration space

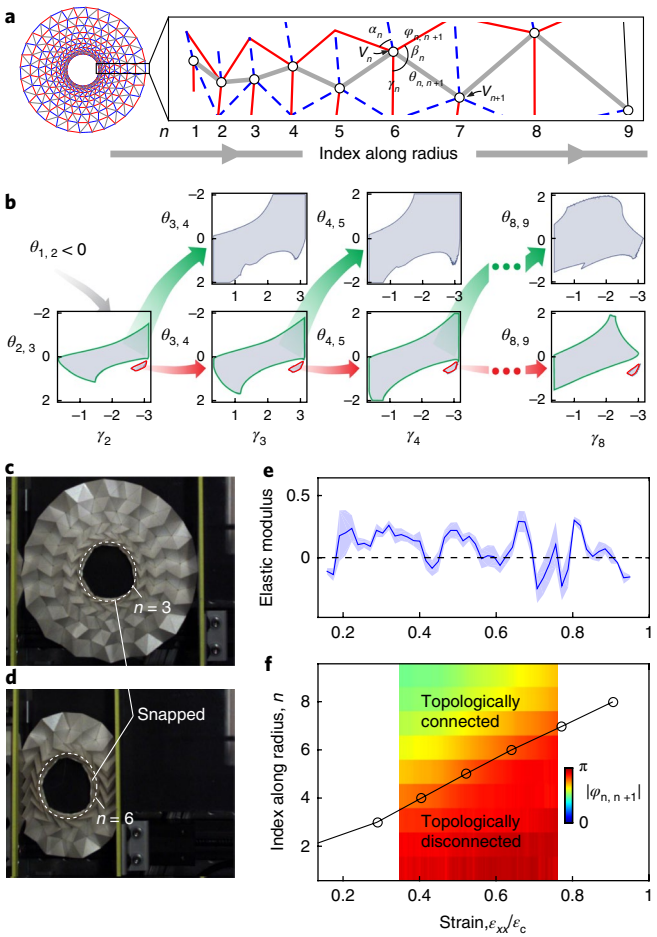

Fig. 3 | Coupling configuration-space topology with vertex–vertex interactions. a, Folding diagram for a Miura-ori ring and definition of the fold angles $\theta_{n,n+1}$ and γ_n. The geometry consists of triangulated Miura-ori vertices (Fig. 2a) connected such that α_n and $\beta_n = \pi - \alpha_n$ vary as a function of indexed position along the ring radius. The resulting configuration space includes pure-crease DOFs (red, blue lines) as well as facet-bending DOFs (grey lines) all operating at the same energy scale. **b**, For all $\theta_{1,2} < 0$, the configuration space $\langle \gamma_2, \theta_{2,3} \rangle$ is topologically disconnected. Configurations in the larger region (outlined green) lead to configurations at the next vertex ($\langle \gamma_3, \theta_{3,4} \rangle$) that are topologically connected. Configurations in the smaller region (outlined red) lead to configurations at the next vertex ($\langle \gamma_3, \theta_{3,4} \rangle$) that are topologically disconnected. This pattern of coupling configuration-space topology continues along the radial index n due to vertex–vertex interactions. **c**,**d**, An experimentally fabricated Miura-ori ring (**c**) is compressed using a controlled strain measurement device (**d**). The mechanical actuation drives the structure through series of topologically disconnected configurations depicted in the lower row of **b**. **e**, The compressive elastic modulus of the Miura-ori ring as a function of normalized strain ϵ_{xx}/ϵ_c, where the critical strain $\epsilon_c = 0.75$ and corresponds to the strain at which the entire sheet snaps into a cylindrical wall, is obtained from the force–strain measurement (see Supplementary Information). The modulus shows a sequence of drops in its value, each of which corresponds to a bistability snap. The blue line is a ten-point boxcar average of the measured modulus value and the shaded band is the ten-point boxcar standard deviation. **f**, Quantitative image analysis measures the folding angle $\varphi_{n,n+1}$, which correlates with the configuration-space topology of each vertex. At the lowest measured strain, vertices with $n \leq 4$ have been driven into the topologically disconnected configuration spaces, whereas vertices with $n > 4$ still have topologically connected configuration spaces. The solid line shows the boundary between the vertices with topologically connected configuration spaces and the vertices with topologically disconnected configuration spaces (see Supplementary Information).

with a topological bistability (Fig. 3b, $\langle \gamma_2, \theta_{2,3} \rangle$, disconnected green and red regions). As the structure is further folded, each vertex in the second ring moves through configuration space, and ultimately transitions across the topological bistability (Fig. 3b, moving from the green region to red region). In the mathematical abstraction of configuration space (Fig. 1a, right-most motif), this transition is strictly forbidden. However, in experimental systems, the transition becomes possible when hidden DOFs are invoked to bridge the topological gap (Fig. 1a, centre motif). When the second ring crosses the bistability transition, this newly occupied region of configuration space constrains the third ring so that its previously connected configuration space (Fig. 3b, upper $\langle \gamma_3, \theta_{3,4} \rangle$ configuration space) now exhibits a topological bistability (Fig. 3b, lower $\langle \gamma_3, \theta_{3,4} \rangle$ configuration space). This process repeats across the entire structure; as each ring crosses a topological bistability, it generates constraints that introduce topological bistability in the next ring of the sequence (Fig. 3b, configuration-space diagrams read left-to-right). In practice, we therefore expect that a physical Miura-ori ring that contains hidden DOFs will undergo a sequential series of snaps as the structure is folded and each ring transitions through its respective topological bistability via energetic deformations not described by the configuration-space topology. We experimentally fabricated this structure (Fig. 3c,d), measured its force–displacement relation as the structure was folded (Methods), and confirmed the expected bulk phenomenology (Fig. 3e). Coexistence of the topologically connected and disconnected configuration spaces can be predicted and quantitatively compared with the measurements, which are most conveniently expressed by the crease angle $\phi_{n,n+1}$ (Fig. 3f). While the crease pattern of this structure has apparent similarities with other cyclic origami designs[29–32], the sequence of transitions through topological bistabilities shown here is a significant difference that distinguishes the kinematic behaviour from related flat-foldable and nearly single-DOF structures. As such, these seemingly small differences in folding pattern demonstrate that vertex–vertex coupling has consequential significance by propagating topologically prescribed mechanical effects across the entire structure during folding actuation.

In the Miura-ori ring structure, we showed how folding on one crease can alter the configuration-space topology elsewhere in the structure. Next, we consider the opposite scenario where the global configuration space is disjointed and actuation of a family of creases in one region has no effect in another. For this two-DOF actuation to occur, the configuration-space topology will be separated into two domains that touch only at a single point. One domain in configuration space corresponds to half of the physical structure, while the other domain in configuration space corresponds to the other half of the physical structure. Thus, an actuation in one half of the structure is dimensionally reduced at the interface between the two structures; as the topology of configuration space involves two domains that touch at a single point, the beginning and end points of the path are collapsed onto this point in configuration space. This collapse of the path to a point creates a degeneracy that places no constraints on the allowed configurations within the other half of the structure. As such, any other simply connected path in the other domain is freely realizable, since it too will be dimensionally reduced to the same point in configuration space.

To illustrate this principle in a non-trivial tessellation, we connect a series of vertices such that the parameter α varies in a prescribed fashion for each column (Fig. 4a). If each vertex were isolated from the overall structure, there would be a set of independent configuration spaces (Fig. 4b, grey region in each configuration space diagram). However, vertex–vertex coupling imposes topological constraints (Fig. 4b, shaded pink region) on the accessible configuration space. If we actuate folding at the vertex described by the $\langle \theta_{-5,-4}, \theta_{-4,-3} \rangle$ configuration space (Fig. 4b, arbitrary trace within the topologically allowed region from the red circle to the

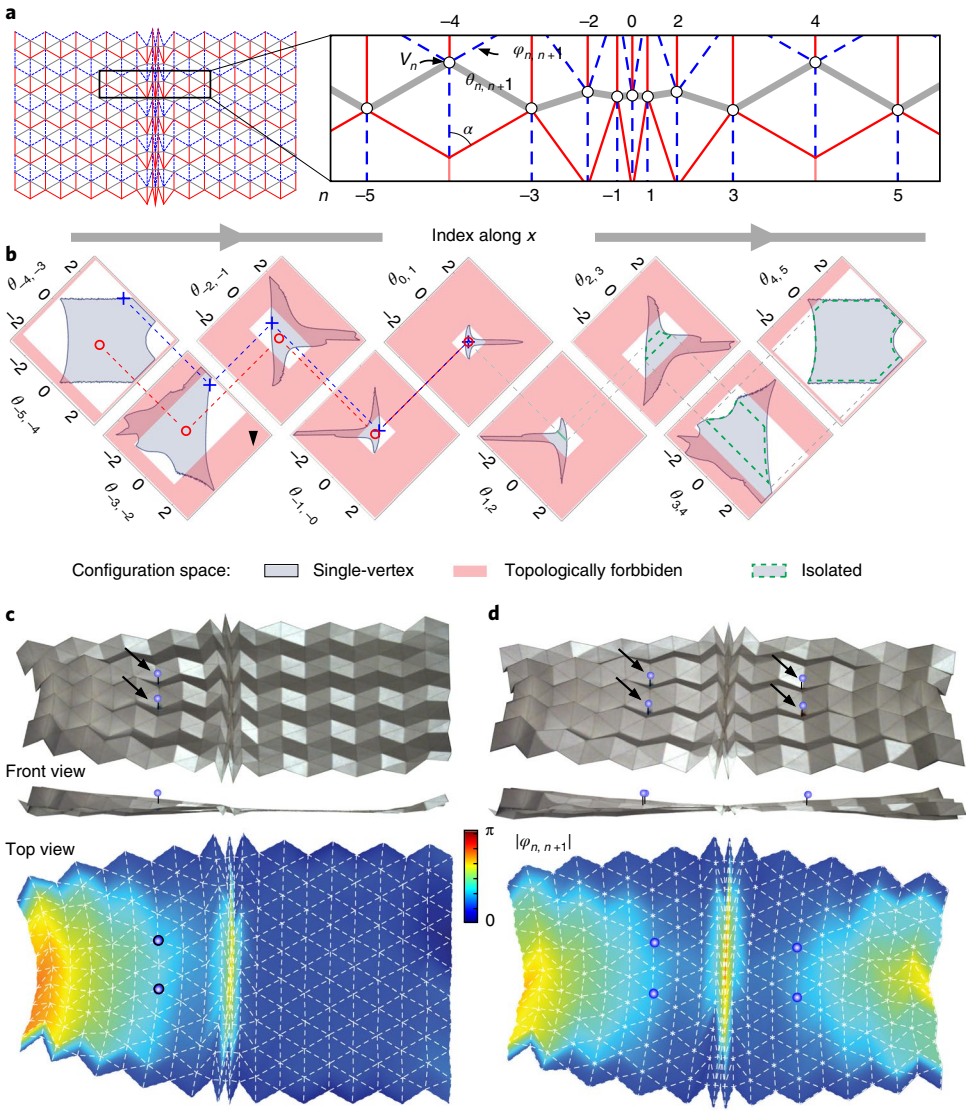

Fig. 4 | Decoupling configuration-space topology with vertex–vertex interactions. a, Folding diagram for a two-DOF Miura-ori-like structure and definition of the fold angles $\theta_{n,n+1}$. The geometry consists of triangulated Miura-ori vertices (Fig. 2a) connected such that α_n vary as a function of indexed position along the x axis. The resulting configuration space includes pure-crease DOFs (red, blue lines) as well as facet-bending DOFs (grey lines) all operating at the same energy scale. **b**, Isolated vertices have allowed configuration spaces $\langle\theta_{n-1,n}, \theta_{n,n+1}\rangle$ (grey shaded regions); however, when connected, regions of configuration space become topologically forbidden (red shaded regions). Nevertheless, deformations between $n<0$ and $n>0$ are decoupled. For example, a path between two points in the $\langle\theta_{-5,-4}, \theta_{-4,-3}\rangle$ configuration space has a corresponding path in the configuration spaces $\langle\theta_{-4,-3}, \theta_{-3,-2}\rangle$, $\langle\theta_{-3,-2}, \theta_{-2,-1}\rangle$ and $\langle\theta_{-2,-1}, \theta_{-1,0}\rangle$. This path collapses to a single point in the $\langle\theta_{-1,0}, \theta_{0,1}\rangle$ configuration space, which permits a variety of configurations for the vertices with increasing index (green isolated regions). As n increases, the constraints on configuration space rapidly vanish, decoupling deformations between $n<0$ and $n>0$. **c**,**d**, The experimentally fabricated structure is pinched at two points (**c**) and four points (**d**) on either side of $n=0$ (top), leading to strain fields (bottom) that are decoupled by the crease pattern at $n=0$.

blue cross), then the neighbouring vertices to the right will undergo an actuation within their own topologically allowed configuration space. In the configuration space $\langle\theta_{-1,0}, \theta_{0,1}\rangle$, the end points of these paths collapse onto a single point that allows for a range of configurations for the vertices further to the right (Fig. 4b, regions of configuration spaces within the green dashed lines). In fact, the configuration space $\langle\theta_{3,4}, \theta_{4,5}\rangle$ is essentially unconstrained by the path in the $\langle\theta_{-1,0}, \theta_{0,1}\rangle$ configuration space, and any effects from actuation in the left half of the tessellation are suppressed in the right half of the tessellation. In essence, the configuration spaces on the left and right portions of this structure are disconnected. We experimentally fabricated this tessellation and found that we could independently actuate the left and right halves as expected (Fig. 4c,d). Hence, vertex–vertex coupling in this structure allows us to decouple the configuration-space topology in a manner that allows for localization of real-space kinematics. Importantly, this design can be treated as a modular structure and combined with the Miura-ori ring to create larger composite structures where the configuration-space constraints act locally on each module.

Origami-inspired metamaterials have a number of desirable features including single-sheet fabrication, compatibility with well-established self-assembly methods, and an essentially infinite design space associated with the rich variety of folding patterns. Here, we have added to this list the capacity to design kinematic properties from the configuration-space topology that can be modularly assembled as constituents of a larger structure. This approach to

metamaterial design produces structures with regions that are physically attached to one another but kinematically isolated through constraints on their configuration space. In applications, the benefits of our findings allow for the design of structures insensitive to real-world manufacturing defects and tolerances[23,33,34]. This flexibility can be potentially achieved by incorporating known imperfections as added volume into the analysis of configuration-space topology, ensuring the folding actuations are as intended. From this perspective, monostability and bistability can be robustly designed even in the presence of parasitic compliance. With the results presented here, it becomes possible to design topologically constrained metamaterials with well-defined properties even in the presence of irregular or unpredictable forces. Such devices are particularly exciting at the meso- and microscale for applications in biological fluid flow and tissue engineering.

Methods

Methods, including statements of data availability and any associated accession codes and references, are available at https://doi.org/10.1038/s41567-018-0150-8.

Received: 15 October 2017; Accepted: 19 April 2018;
Published online: 28 May 2018

References

1. Qi, X.-L. & Zhang, S.-C. Topological insulators and superconductors. *Rev. Mod. Phys.* **83**, 1057–1110 (2011).
2. Bader, R. & Nguyen-Dang, T. T. A topological theory of molecular structure. *Rep. Prog. Phys.* **44**, 893–948 (1981).
3. Avron, J. E., Osadchy, D. & Seiler, R. A topological look at the quantum Hall effect. *Phys. Today* **56**, 38–42 (2003).
4. Lu, L., Joannopoulos, J. D. & Soljačić, M. Topological photonics. *Nat. Photon.* **8**, 821–829 (2014).
5. Kane, C. L. & Lubensky, T. C. Topological boundary modes in isostatic lattices. *Nat. Phys.* **10**, 39–45 (2013).
6. Paulose, J., Chen, B. G.-g & Vitelli, V. Topological modes bound to dislocations in mechanical metamaterials. *Nat. Phys.* **11**, 153–156 (2015).
7. Mahadevan, L. & Rica, S. Self-organized origami. *Science* **307**, 1740–1740 (2005).
8. Schenk, M. & Guest, S. D. Geometry of Miura-folded metamaterials. *Proc. Natl Acad. Sci. USA* **110**, 3276–3281 (2013).
9. Wei, Z. Y., Guo, Z. V., Dudte, L., Liang, H. Y. & Mahadevan, L. Geometric mechanics of periodic pleated origami. *Phys. Rev. Lett.* **110** (2013).
10. Silverberg, J. L. et al. Using origami design principles to fold reprogrammable mechanical metamaterials. *Science* **345**, 647–650 (2014).
11. Yasuda, H. & Yang, J. Reentrant origami-based metamaterials with negative Poisson's ratio and bistability. *Phys. Rev. Lett.* **114**, 185502 (2015).
12. Filipov, E. T., Tachi, T. & Paulino, G. H. Origami tubes assembled into stiff, yet reconfigurable structures and metamaterials. *Proc. Natl Acad. Sci. USA* **112**, 12321–12326 (2015).
13. Giampieri, A., Perego, U. & Borsari, R. A constitutive model for the mechanical response of the folding of creased paperboard. *Int. J. Solids Struct.* **48**, 2275–2287 (2011).
14. Lechenault, F., Thiria, B. & Adda-Bedia, M. Mechanical response of a creased sheet. *Phys. Rev. Lett.* **112**, 244301 (2014).
15. Hull, T. *Project Origami: Activities for Exploring Mathematics*. (CRC Press: Boca Raton, FL, 2006).
16. Silverberg, J. L. et al. Origami structures with a critical transition to bistability arising from hidden degrees of freedom. *Nat. Mater.* **14**, 389–393 (2015).
17. Chen, B. G.-g et al. Topological mechanics of origami and kirigami. *Phys. Rev. Lett.* **116**, 135501 (2016).
18. Hanna, B. H., Lund, J. M., Lang, R. J., Magleby, S. P. & Howell, L. L. Waterbomb base: a symmetric single-vertex bistable origami mechanism. *Smart Mater. Struct.* **23**, 094009 (2014).
19. Waitukaitis, S., Menaut, R., Chen, B. G.-g & van Hecke, M. Origami multistability: from single vertices to metasheets. *Phys. Rev. Lett.* **114**, 055503 (2015).
20. Yang, N. & Silverberg, J. L. Decoupling local mechanics from large-scale structure in modular metamaterials. *Proc. Natl Acad. Sci. USA* **114**, 3590–3595 (2017).
21. Brunck, V., Lechenault, F., Reid, A. & Adda-Bedia, M. Elastic theory of origami-based metamaterials. *Phys. Rev. E* **93**, 033005 (2016).
22. Waitukaitis, S. & van Hecke, M. Origami building blocks: Generic and special four-vertices. *Phys. Rev. E* **93**, 023003 (2016).
23. Tachi, T. Rigid-foldable thick origami. In *Origami 5: The 5th International Conference on Origami in Science Mathematics and Education* (eds Wang-Iverson, P. et al.) 253–264 (Taylor & Francis, New York, NY, 2011).
24. Evans, A. A., Silverberg, J. L. & Santangelo, C. D. Lattice mechanics of origami tessellations. *Phys. Rev. E* **92**, 013205 (2015).
25. Miura, K. Method of packaging and deployment of large membranes in space. *Inst. Space Astronaut. Sci. Rep.* **618**, 1–9 (1985).
26. Nakahara, M. *Geometry, Topology and Physics* 2nd edn (Taylor & Francis, Boca Raton, FL, 2003).
27. Nojima, T. *Origami Modeling of Functional Structures Based on Organic Patterns*. MSc thesis, Kyoto Univ. (2002).
28. Tachi, T. Designing freeform origami tessellations by generalizing Resch's patterns. *J. Mech. Des.* **135**, 111006 (2013).
29. Barreto, P. T. Lines meeting on a surface: the "Mars" paperfolding. In *Proc. 2nd International Meeting of Origami Science and Scientific Origami* 323–331 (ed. Miura, K.) (Sein Univ. Art and Design, Otsu, 1997).
30. Nojima, T. Modelling of folding patterns in flat membranes and cylinders by origami. *JSME Int. J. Ser. C* **45**, 364–370 (2002).
31. Lang, R. J. The science of origami. *Phys. World* **20**, 30 (2007).
32. Kovac, M. & Sareh, P. Aerial devices capable of controlled flight. WO patent application PCT/GB2016/051,567 (2016); https://www.google.com/patents/WO2016193690A1?cl=en
33. Francis, K. C. et al. From crease pattern to product: considerations to engineering origami-adapted designs. In *Proc. ASME 2014 IEDTC & CIEC, Buffalo, NY, 17–20 August 2014*, V05BT08A030 (ASME, New York, NY, 2014).
34. Chen, Y., Peng, R. & You, Z. Origami of thick panels. *Science* **349**, 396–400 (2015).

Acknowledgements

The authors thank A. Ruina, T. Healy, J. Jenkins, U. Nguyen, L. Freni and the Cohen laboratory for useful discussions. We also thank F. Parish for assistance with the laser cutter, and S. Waitukaitis, P. Dieleman and M. van Hecke for providing the photo in Fig. 1b. This work was supported by the National Science Foundation grant no. EFRI ODISSEI-1240441. I.C. received continuing support from DMREF-1435829. B.L. acknowledges the support of the National Science Foundation grant no. NSF CBET-1706511. C.D.S. acknowledges the kind hospitality of the Kavli Institute of Theoretical Physics in Santa Barbara, CA, funded by the National Science Foundation under grant no. NSF PHY-1125915.

Author contributions

B.L. and J.L.S. designed the research; B.L. conducted the research; B.L., J.L.S., A.A.E., R.J.L., T.C.H. and I.C. interpreted the results; C.D.S., R.J.L., T.C.H. and I.C. supervised the research; B.L., J.L.S., C.D.S., R.J.L., T.C.H. and I.C. prepared the manuscript.

Competing interests

The authors declare no competing interests.

Additional information

Supplementary information is available for this paper at https://doi.org/10.1038/s41567-018-0150-8.

Reprints and permissions information is available at www.nature.com/reprints.

Correspondence and requests for materials should be addressed to B.L.

Publisher's note: Springer Nature remains neutral with regard to jurisdictional claims in published maps and institutional affiliations.

Methods

3D model of origami structures. A mathematical model of each experimentally generated origami structure is formulated for numerical simulation and 3D reconstruction. The model is composed of the vertex coordinates and the constraints imposed by the crease length between neighbouring vertices. Given a 2D projection of all the vertex positions (x_i, y_i), the z_i coordinates in the third dimension are obtained by minimizing a penalty function[28] $V(z)=\frac{k}{2}\sum_{i,j}{}'\,[\sqrt{(x_i-x_j)^2+(y_i-y_j)^2+(z_i-z_j)^2}-l_{ij}]^2$, where l_{ij} is the length of the crease between two connected vertices of indices i and j on the triangular crease lattice. The z coordinates can thus be obtained by solving the associated ordinary differential equation array as $\dot{z}_i=-k\sum_j{}'\,[\sqrt{(x_i-x_j)^2+(y_i-y_j)^2+(z_i-z_j)^2}-l_{ij}]\,\hat{r}_{ij}\cdot\hat{z}$, where the unit vector $\hat{r}_{ij}=((x_i-x_j)\hat{x}+(y_i-y_j)\hat{z}+(z_i-z_j)\hat{z})/\sqrt{(x_i-x_j)^2+(y_i-y_j)^2+(z_i-z_j)^2}$ and k is the virtual spring constant for perturbing the crease lengths. The ambiguity due to mountain–valley crease alignments is avoided by shifting the vertices up or down by a small amount in the z direction as the initial condition.

Configuration-space analysis. The configuration space of each vertex is described by the accessible folding angles of the connected creases. In the case of a degree-6 vertex, the configuration space is 3D. Any potentially foldable structure is realized by rotating the creases through those three independent folding angles. The foldability is validated by the criterion that the distance between any pair of transformed vertices cannot be greater than that in the flat unfolded state for any inextensible sheet. Self-intersections of the structures are also identified and excluded from the configuration space (see Supplementary Information). The numeric code for the configuration-space analysis is made available for sharing through Mathematica (https://www.wolframcloud.com/objects/6a35243a-e7ba-479f-af5d-0d77e13f467b).

Experiments. The origami structures described in the main text were made from a flat paper sheet (Stardream Metallics 81lb) with measured thickness $\tau=0.16$ mm and flexural rigidity $D=4.0\times10^{-4}$ N m (ref. [16]). The crease lines were perforated by a laser cutter and weakened manually by flat-folding along the perforation lines in both directions. Folding kinematics and vertex locations were recorded by a USB digital camera (Imaging Source DFK), which was calibrated to remove perspective and lens distortions. The (x, y) coordinates of the vertices were fed into the aforementioned mathematical model to extract the z positions of the vertices. 3D configurations of the folded origami sheets were then reconstructed and plotted using MATLAB.

Data availability. The data that support the plots within this paper and other findings of this study are available from the corresponding author upon request.